C. R. Physique 13 (2012) 293–306

Contents lists available at SciVerse ScienceDirect

Comptes Rendus Physique

www.sciencedirect.com

Use of large scale facilities for research in metallurgy

X-ray line profiles analysis of plastically deformed metals

Profils de raie en rayons X sur des matériaux métalliques déformés plastiquement

András Borbély [a,*], Tamás Ungár [b]

[a] *SMS Materials Centre and CNRS UMR 5146, École des mines de Saint Etienne, 158, cours Fauriel, 42023 Saint Etienne, France*
[b] *Department of Materials Physics, Eötvös University Budapest, P.O. Box 32, Budapest H-1518, Hungary*

ARTICLE INFO

Article history:
Available online 28 January 2012

Keywords:
Metals and alloys
X-ray diffraction
Line profile analysis
Dislocation density
Planar faults

Mots-clés :
Métaux et alliages
Diffraction des rayons *X*
Analyse des profils de raie
Densité de dislocations
Défauts planaires

ABSTRACT

The theoretical basis of X-ray line profile analysis and its application to microstructural characterization of plastically deformed metallic alloys is presented. The microstructure is described in terms of coherent domain size, planar fault density, dislocation density and a dislocation arrangement parameter. Two evaluation methods are introduced: the momentum method and the extended Convolutional Multiple Whole Profile fit procedure. Their use is exemplified on plastically deformed single crystals, single grains residing in the bulk of a polycrystal and family of grains making up texture components. The selected examples show the potential of X-ray line profile analysis applied to diffraction patterns recorded with laboratory or synchrotron sources.

RÉSUMÉ

Nous présentons la base théorique de l'analyse des profils de raie en rayons X, et son application à la caractérisation microstructurale de métaux déformés plastiquement. La microstructure est décrite en termes de taille de domaine cohérent, densité de défauts planaires, densité de dislocations et un paramètre d'arrangement des dislocations. Nous introduisons deux méthodes d'analyse : la méthode des moments, et la méthode étendue d'ajustement par analyse *Convolutional Multiple Whole Profile*. Nous présentons des exemples d'utilisation de ces mesures sur la déformation plastique de monocristaux, de monocristaux résidant dans le volume d'un polycristal, et dans le cas de familles de grains constituant des composantes de texture. Les exemples sélectionnés montrent le potentiel de la technique d'analyse du profil de raies obtenues soit par des sources de laboratoire ou par rayonnement synchrotron.

1. Introduction

Diffraction peaks broaden when crystallites become small and/or atoms are displaced from their ideal position due to lattice defects. The art of correlating diffraction patterns and crystal defects is called: line profile analysis. Fundamentally two different approaches have been developed during the last, about nine decades. The *top-down* approach operates with well-defined analytical functions fitted to the measured diffraction patterns [1–8]. The *bottom-up* approach starts from

* Corresponding author.
E-mail address: borbely@emse.fr (A. Borbély).

1631-0705/$ – see front matter
doi:10.1016/j.crhy.2011.12.004

the displacement field of lattice defects and calculates the corresponding intensity distributions by analytical [9–24] or numerical [25] methods.

Line profile analysis is an indirect method for determining the microstructure of crystalline materials in which sense it can be considered as the counterpart of the different electron microscopy methods. Despite its indirect nature line profile analysis proves to be a valuable and powerful method providing quantitative complementary information of several microstructure parameters. In the present work the basic principles of line profile analysis are summarized and practical aspects of the evaluations are highlighted. Emphasis is made on the momentum method [20] and on the extended Convolutional Multiple Whole Profile (eCMWP) method [26–30]. An existing software package allows evaluating different diffraction patterns measured on different crystalline materials: powders, bulk polycrystals, single-crystalline or textured specimens. For example, in the case of single crystals [30–33] or single grains [34,35], the individual diffraction profiles of different Bragg reflections can be analyzed in terms of individual dislocation contrast factors. Or, in the case of an ideally random powder specimen, the whole measured powder pattern can be evaluated with the same philosophy as the structure refinement by the Rietveld method, however by using lattice-defect related profile functions [36–39]. In this case the whole measured pattern is fitted by a theoretically constructed diffraction pattern which is expressed in terms of dislocation structure parameters, the average dislocation contrast factors, coherent domain size and size-distribution functions as well as in terms of planar-fault densities. The theoretical diffraction patterns are constructed from defect related profile functions. Strain profiles are derived for dislocated crystals by using the theoretical results of Krivoglaz [12,13], Wilkens [14,15], Gaál [16] and Groma [17]. Size profiles are calculated by using fundamental optical principles [39] and the concept of column length [11]. Size distribution is taken into account by assuming the log-normal density distribution function for the coherent domain size [23,27,40–45]. The profiles of planar defects are shown to be the sum of symmetrical and anti-symmetrical Lorentzian functions [20,22–24,28,29]. Defect related profile functions derived on the basis of well established physical principles are given by the absolutely necessary, fewest possible number of parameters. The following section provides an overview of these basic principles and presents the main equations of the methods.

2. X-ray line broadening due to crystalline defects

Generally crystal defects in a solid create a specific distortion of the lattice that is characteristic for the fault. Defects are usually classified according to their geometrical extension: point like, linear, planar or volumetric. As most common point defects we mention the interstitial atoms and vacancies. Dislocations and disclinations are line defects, while stacking faults, twins and grain boundaries are examples of planar defects. Finally, atomic clusters and precipitates are identified as volumetric or bulk defects. Each defect distorts the lattice in its neighborhood in a characteristic way leading to different line profile shape and very often to *hkl* dependent broadening. This characteristic broadening is the basis for obtaining information on the nature and density of defects. For example point defects distort the lattice only over a distance of a few atomic spacing, giving a measurable intensity contribution only far from the center of Bragg peaks. As we focus our attention on crystal defects that are influencing the shape of the Bragg peaks point defects are not studied here. Our analysis concerns diffraction line broadening caused by coherent domain size (due to existence of grain/subgrain boundaries), dislocations, planar faults as well as the combined case when all of these faults are present in different proportions.

2.1. Broadening due to small coherent domain size

The simplest type of line broadening is related to the small crystallite size, when the diffracting matter has a perfect crystalline structure, but the Bragg peaks broaden due to the small number of atoms (limited by grain/subgrain boundaries) participating to constructive interference. The Fourier transform of the intensity distribution in this case is proportional to the auto-correlation function of the domain shape, i.e. the common volume between the original domain and the one shifted by the Fourier parameter in the direction of the diffraction vector. The asymptotic behavior of the interference function at large q values measured from peak center ($q = 2(\sin(\theta) - \sin(\theta_0))/\lambda$, where λ is the wavelength of the X-ray, θ is the diffraction and θ_0 is the Bragg angle) is proportional to q^{-2} [45]. Therefore the intensity distribution is usually approximated by a Cauchy–Lorentz [41] function, which has identical asymptotic behavior. Based on this property it was shown by Wilson [45] that the asymptotic behavior of the variance of the line profile becomes a linear function of q:

$$M_2(q) = \frac{1}{\pi^2 \varepsilon_F} q - \frac{T}{4\pi^2 K^2 \varepsilon_F^2} \tag{1}$$

where ε_F is the area weighted particle size measured in the direction of the diffraction vector, K is the Scherrer constant and T is the so-called taper parameter depending on the rate of the decrease of the cross-sectional area of the crystallites [45–47]. Both K and T are functions of the diffraction order *hkl* and particle shape [45,48]. If the domain size has a distribution the scattered intensity is the weighted average of the intensity profiles created by domains of different size. Although, the direct formulation of the problem is relatively simple, the inverse problem of the determination of the grain size distribution from a measured X-ray pattern is still a challenge. Bertaut proved [11] that it is possible to determine the column-length distribution from the second derivative of the size Fourier coefficients. Due to unavoidable scatter and truncation of the data, application of the second order derivative in practice remains, however, difficult. To facilitate automatic

fitting several works are postulating a priori size-distribution functions, reducing the distribution problem to the determination of the mean and variance of the selected function. Since a selected size distribution function cannot be generalized to all specimens the subject will not be treated here and we refer the reader to the vast scientific literature [27,40–44,49,50].

2.2. Planar defects

Profile functions for stacking faults and twinning cannot be given in a straightforward manner. The reason for this is that the line profiles of faulted and twinned crystals consist of several sub-profiles, where their number depends on *hkl* indices, and for special *hkl* indices the sub-profiles can be delta functions [21–25,28,29]. For the case of *fcc* crystals, when faulting or twinning occurs on the close packed planes Estevez-Rams and coauthors [22,24] have developed a Fourier method in which the Fourier coefficients of the physical profiles were directly compared with Fourier coefficients calculated for model crystals containing stacking faults. This method was generalized by Balogh et al. [28,29] by showing that the diffraction profiles in a powder pattern can be given as the sum of a symmetric and an anti-symmetric component. The Fourier coefficients of these two function components were determined as a function of faulting parameters and incorporated into the framework of a whole powder pattern fitting procedure. Velterop et al. [21] developed analytical expressions for the breadths and shifts of profile functions for faulted and twinned crystals as a function of fault densities, however, only for *fcc* materials with faulting on the close packed planes.

Twinning in hexagonal metals, especially in Ti, Mg and Zr and their alloys, occurs on pyramidal planes. Most frequently observed twinning systems are the $\{10.1\}\langle 10.\bar{2}\rangle$ and $\{11.2\}\langle 11.\bar{3}\rangle$ as compressive, and the $\{10.2\}\langle 10.\bar{1}\rangle$ and $\{11.1\}\langle \bar{1}\bar{1}.6\rangle$ systems as tensile [51,52]. It has been shown in [29] that the general theory for twinning on close packed planes of *fcc* crystals, cf. [21–25,28] cannot be applied to twinning on the pyramidal planes in *hcp* materials. The reason for this is that twinning in *fcc* crystals is *partially-merohedral*, whereas on pyramidal planes of *hcp* materials it is *non-merohedral* [53]. In the case of *fcc* crystals *partial merohedry* means that each third plane is repeating itself in the direction normal to the twinning plane. In the case of *hcp* materials, however, repetition of lattice planes in the twinning direction never occurs, unless the c/a ratio fulfills some very specific conditions. This is called *non-merohedry*.

Balogh and coworkers worked out a method in which the breadths and shifts of sub-profiles are parameterized as functions of the twin and stacking-fault densities for the different fault planes either for *fcc* [28] or for *hcp* [29] crystals. Powder diffraction patterns were numerically calculated by using the DIFFaX [25] software for intrinsic and extrinsic stacking faults, and twin boundaries in *fcc* crystals [28] and for the most common compressive and tensile twin systems in *hcp* materials [29]. The numerical calculations were carried out for a large number of Bragg reflections up to very high fault densities. The shape of sub-profiles was derived theoretically to be the sum of a symmetrical and anti-symmetrical Lorentzian function [29] in good correlation with the results of Estevez-Rams et al. [22,24]. It was shown that the anti-symmetrical Lorentz function is the consequence of interference between two overlapping sub-reflections in reciprocal space. The symmetrical and anti-symmetrical parts of the sub-reflections are strictly correlated and can be characterized by the breadth, $FWHM_{tri}$, and the anti-symmetry parameter, A_{tri}, along the streaking direction L in reciprocal space (Eq. (28) in [29]). The $FWHM_{tri}$ and A_{tri} values can be parameterized as a function of fault density for the different stacking faults and twins and are available through the web [54]. Typical profiles for two Ti sub-reflections, $\bar{1}2\bar{1}4$ and $\bar{3}030$ with $\beta = 4\%$ twinning on the $11\bar{2}2$ plane as calculated by the DIFFaX software (open circles) and the corresponding symmetrical (black line) and anti-symmetrical (red line) Lorentzian profile functions (solid line) are shown in Fig. 1. The profile function corresponding to the sum of these two Lorentzian functions is the blue curve matching the numerically calculated open circles with high accuracy. Due to this Lorentzian shape twins and stacking faults are seen by the variance method as a general particle type broadening. The evidence about existing planar defects is obtained in a second step from the analysis of several peaks [55].

2.3. Dislocations induced line broadening

The first theory of line broadening due to crystal defects was proposed by Warren and Averbach [10,55,56]. Their model aims to be very general for which reason does not take into account the specific type of the defects. From the Taylor expansion of the Fourier transform of the line profile the Warren–Averbach (WA) model states that broadening scales with the spatial average of the mean square strain $\langle \varepsilon^2 \rangle$. Warren suggested two models for the dependence of $\langle \varepsilon^2 \rangle$ with the Fourier length L: (i) one with $\langle \varepsilon^2 \rangle = \text{constant}$, and another (ii) with $\langle \varepsilon^2 \rangle \approx 1/(1 + L^2)$. In the first case the line profile is of Gaussian type, whereas in the second case is Lorentzian. Linear type lattice defects such as dislocations give rise profile shapes which are neither of Lorentzian nor of Gaussian functions.

Krivoglaz calculated $\langle \varepsilon^2 \rangle$ for dislocated crystals by assuming randomly distributed dislocations [12,13]:

$$\langle \varepsilon_L^2 \rangle \cong \frac{\rho C b^2}{4\pi} \ln \frac{L}{D} \tag{2}$$

where ρ, C and b are the average density, the contrast factor and the Burgers vector of dislocations, respectively. In the logarithmic term D is the size of the crystal. As shown later by Wilkens [15] this model cannot be applied to dislocations since in this case $\langle \varepsilon_L^2 \rangle$ diverges logarithmically with the specimen size. The divergence is a consequence of the long-range $1/r$ type decay of the strain field created by dislocations. Wilkens recognized that in order to lift the divergence related to the crystal size, real dislocation arrangements must be correlated [15]. He developed the model of *restrictedly random*

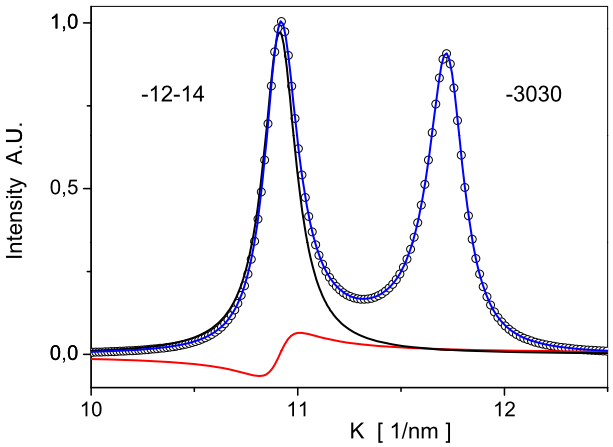

Fig. 1. The intensity distributions of the two Ti sub-reflections, $(\bar{1}2\bar{1}4)$ and $(\bar{3}030)$, for $\beta = 4\%$ twinning on the $(11\bar{2}2)$ plane calculated by the DIFFaX software (open circles) and the fitting by a function of which the mathematical form is given by Eq. (28) in [29] (blue solid line). The black and red lines are for the symmetrical and anti-symmetrical Lorentzian contributions to the $(\bar{1}2\bar{1}4)$ sub-reflection, respectively. (By courtesy of [29].) (For interpretation of the references to color in this figure, the reader is referred to the web version of this article.)

distribution of dislocations and worked out an analytical function describing the Fourier transform of the line profile [15]. The restricted randomness in the Wilkens' model means that the section of a sample can be subdivided into areas of size A which are intersected by identical number of dislocations $N_A = \rho A$, where ρ is the dislocation density. Since the Fourier transform of the intensity distribution for this special type of dislocation arrangement is available in closed form, this model is currently at the basis of several modeling techniques built on the ideas of Rietveld refinement [23,30]. Correlations in dislocation arrangement have been also found responsible for line broadening measured on heteroepitaxial structures [57]. Wilkens modified the expression of $\langle \varepsilon_L^2 \rangle$ as:

$$\langle \varepsilon_L^2 \rangle = \frac{\rho C b^2}{4\pi} f(L/R_e) \tag{3}$$

where R_e is the effective outer cut-off radius of dislocations and $f(L/R_e)$ is the Wilkens function, shown in Fig. 2(a), where $\eta = L/R_e$. At small or large η values the $f(\eta)$ function is asymptotically logarithmic or hyperbolic, respectively [15]. The dash–double-dot line stands for the logarithmic part, whereas the dashed line is for the hyperbolic part. The solid curve is the $f(\eta)$ function correct in the entire η range. This function is not analytical and can only be given numerically [15]. Since the actual value of R_e is coupled to dislocation density, Wilkens introduced the dimensionless parameter $M = R_e\sqrt{\rho}$ for characterizing the dislocation arrangement. If the screening of the strain fields is strong or weak in the dislocation ensemble the value of M will be smaller or larger than unity. The effect of the strength of the screening in the profile shape can be visualized in a simple manner. A strong or weak screening means that the strain fields decay faster or slower. Since diffraction is manifested in the reciprocal space, the faster or slower decaying strain fields will correspond to longer or shorter tails in the peak profiles, as shown in Fig. 2(b). The two profiles are normalized by the maximum intensity and by the FWHM measured in reciprocal-space coordinates. The figure shows that for strong or weak screening the M parameter becomes smaller or larger than unity. The corresponding profile shapes will be then closer to a Lorentzian or Gaussian type function, respectively. It is noted, however, that profile functions corresponding to realistic dislocation ensembles never reveal purely Lorentzian or Gaussian shape [18,31,32,58].

The general approach to describe dislocation induced line broadening relies on the asymptotic behavior of the intensity distribution, where the functional form of the Fourier coefficients [17,18] or that of restricted moments [19] can be analytically calculated. The theoretically derived model functions containing just a few parameters show an extremely good agreement with experimental data obtained for plastically deformed copper single crystals [59–61]. This general theory of dislocation induced line broadening explains in a straightforward manner the asymmetry of the line profiles, too that is related to the polarization of dislocations arranged in dipoles or dipolar walls [62]. A separate interpretation of the asymmetry of the line profile has been given previously on the basis of the composite model of heterogeneous dislocation structures in terms of long-range internal stresses existing in dislocation cell walls and cell interiors [63]. The two approaches have been shown to be identical [18]. Description of this theory is described in the following by combining the resulting equations [19] with the case of small particle size induced broadening (Eq. (1)).

2.4. Coupled broadening

A special dislocation structure formed during plastic deformation is that of dislocation walls where all dislocations have the same Burgers vector. These polarized tilt walls induce a small relative misorientation between nearby crystal zones and lead to a crystal broken up in small mosaic blocks [64]. The orientation properties of the broken domains are usually

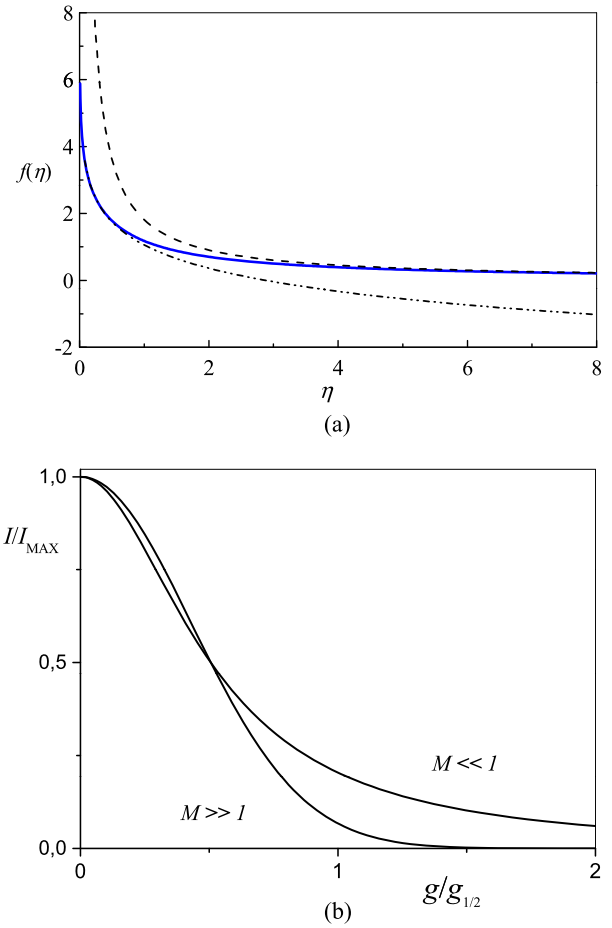

Fig. 2. The Wilkens-function, $f(\eta)$ (a). The dash–double-dot line stands for the logarithmic part which describes the asymptotic behavior at small η values. The dashed line is for the hyperbolic part describing the asymptotic behavior at large η values. The blue curve is the $f(\eta)$ function correct in the entire η range [15]. (b) The intensity distribution of the strain-profiles normalized by the peak maximum, I_{MAX} and FWHM, $g_{1/2}$. M is the parameter characterizing the strength of screening in the dislocation ensemble. (For interpretation of the references to color in this figure, the reader is referred to the web version of this article.)

analyzed by X-ray rocking curve measurements [65] or electron backscatter diffraction [66]. The consequence of the induced misorientation is that coherent diffraction remains limited to single mosaic blocks and as their size becomes smaller than of about 1 μm they contribute with an additional broadening to the measured line profile. This means that in case of severely deformed crystals the line profile will be broadened by the combined effect of the strain field of dislocations and that of small crystallite size. Mathematically, this is given by the convolution of the intensity profiles corresponding to particle size and dislocation induced strain broadening. Dealing with such a case is not easy and the adequate description of the system requires the detailed analysis of several diffraction peaks. Two main approaches for the characterization of the dislocation structure and coherent domain size are presented below.

2.4.1. Momentum method

The first method discussed is based on the asymptotic behavior of different order restricted moments of the measured intensity distribution. The corresponding equations have been derived by considering the combined effect of small crystal size [45–47] and dislocation strain on line broadening [19]. They offer a direct possibility to extract the average particle size and average dislocation density from the moments of the measured line profile. It has been shown [20,67] that the asymptotic behaviors of the variance and fourth order moment have the following functional forms:

$$M_2(q) = \frac{1}{\pi^2 \varepsilon_F} q - \frac{L}{4\pi^2 K^2 \varepsilon_F^2} + \frac{\Lambda \langle \rho \rangle \ln(q/q_0)}{2\pi^2} \tag{4}$$

$$\frac{M_4(q)}{q^2} = \frac{1}{3\pi^2 \varepsilon_F} q + \frac{\Lambda \langle \rho \rangle}{4\pi^2} + \frac{3\Lambda \langle \rho \rangle}{(2\pi)^4 q \varepsilon_F} \ln(q/q_1) + \frac{3\Lambda^2 \langle \rho^{(2)} \rangle}{4\pi^4 q^2} \ln^2(q/q_2) \tag{5}$$

Comparing Eq. (4) to Eq. (1) as well as to Eq. (65) of Ref. [19] it becomes evident that the variance of the general line profile is the additive superposition of the variances describing separately peak broadening due to finite particle size and dislocations. The average dislocation density $\langle\rho\rangle$ appears in the third term of Eq. (4) together with a proportionality factor

$$A = \frac{\pi}{2} g^2 b^2 C \tag{6}$$

where g and b are the magnitudes of the diffraction and Burgers vectors, respectively. C represents the dislocation contrast factor and depends on the dislocation type, the operating diffraction vector and the dislocation population of different slip systems [14,15,17,68]. In general, C is different for different diffraction vectors and it can be calculated if the elastic constants of the crystal are known [68]. For powder specimens, due to the extra averaging over diffraction vectors of the same *hkl* order, the contrast factors obey simple rules related to the fourth order invariants of the Miller indices [69, 70].

It is important to emphasize that contrary to its simplicity the application of the momentum method in practice imposes a stringent constraint on the diffraction instrument. As Eqs. (4) and (5) are describing the behavior of the physical profile the measurement must be performed using a high-resolution equipment with negligible instrumental broadening. Due to the finite measurement window it is evident that any deconvolution procedure alters the tails of the peak and consequently the asymptotic behavior of the restricted moments. Minimal conditions are related to the use of monochromators and of a beam with small divergence. Such double- or triple-crystal diffractometers have a very low intensity that in case of heavily deformed samples imposes long counting times. This drastic decrease in intensity can be counterbalanced by adequate optics, for example a graded multilayer parabolic mirror mounted upstream the monochromator or the use of more powerful sources, rotating anode or synchrotron.

2.4.2. Extended convolutional multiple whole profile fitting

The convolutional approach to line profile analysis seems to be a versatile method that avoids numerical difficulties related to the deconvolution procedure. At the same time it is quite general permitting to consider in a straightforward manner many different contributions to peak broadening. The following section describes the freely accessible eCMWP software package [26–29,37] developed for the evaluation of diffraction patterns measured on different crystalline materials: powders, bulk polycrystals, single crystals or textured specimens. For example, in the case of single crystals, the individual diffraction profiles of different Bragg reflections can be analyzed in terms of individual dislocation contrast factors. Or, in the case of a powder specimen, the whole pattern can be evaluated with the same philosophy as the structure refinement in the Rietveld method. eCMWP approximates the whole measured diffraction pattern by theoretically constructed peak profiles, which are expressed in terms of parameters related to the dislocation structure – average dislocation density, dislocation arrangement factor M, average dislocation contrast factor – and to an average crystallite size and size-distribution function as well as to the density of different planar defects. Strain profiles are derived for dislocated crystals by using the theoretical results of Krivoglaz [13], Wilkens [15] and Groma [19]. Size profiles are calculated by using fundamental optical principles [39] and the concept of column length [11]. Size distribution is taken into account by assuming the log-normal size distribution density function. The profiles of planar defects are taken as the sum of symmetrical and anti-symmetrical Lorentzian functions [28,29]. These defect related profile functions are given by the absolutely necessary, fewest possible number of parameters.

3. Applications

3.1. Determination of twin fault density and dislocation type in plastically deformed Mg

The application of the eCMWP procedure is shown for the case of Mg specimens deformed at different temperatures between room temperature and 300 °C in tension up to fracture [71]. The diffraction patterns were measured by a special high resolution X-ray diffractometer dedicated for X-ray line profile analysis. In [71] it was shown that in the as cast state and up to about 100 °C the overwhelming majority of the dislocations is of $\langle \boldsymbol{a} \rangle$ type. At higher temperatures the fraction of $\langle \boldsymbol{c}+\boldsymbol{a} \rangle$ type dislocations is increasing at the cost of $\langle \boldsymbol{a} \rangle$ type dislocations. The systematic application of the eCMWP procedure for the four different twin systems revealed that dominant twinning in the present specimen is: $\{11.1\}\langle \bar{1}\bar{1}.6 \rangle$ tensile twin family. Slip system activity, dislocation density and twin plane frequency are given as a function of the temperature of deformation in Fig. 3, where the twinning frequency β means that the twin planes are separated by a number of $1/\beta$ atomic planes on the average. The figure indicates that most of the twinning is observed at RT. As $\langle \boldsymbol{c}+\boldsymbol{a} \rangle$ type dislocations are activated the frequency of twinning decreases, in correlation with TEM observations [72].

3.2. Characterization of plane strain compressed Al–0.3%Mn single crystals

Plastically deformed single crystals with relatively low strains offer an adequate reference material for checking the predictions of the general theory of X-ray peak broadening. Three crystals with dimensions of $7 \times 7 \times 15$ mm (in ED-TD-ND) were carefully machined by spark erosion from the as grown ingots and deformed in plane strain compression (PSC) in a Schenk servo hydraulic machine. The orientation of the samples was within 1° of the ideal Goss orientation (011)[100].

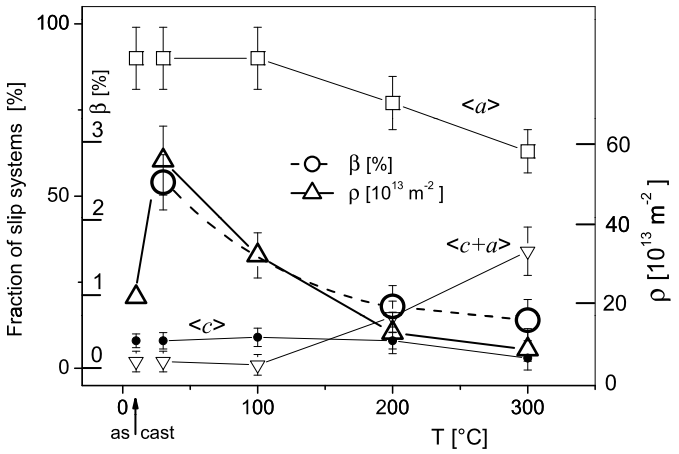

Fig. 3. The fractions of active slip system, dislocation densities and the density of the $\{11.1\}\langle\bar{1}\bar{1}.6\rangle$ tensile twin family versus the temperature of deformation [71].

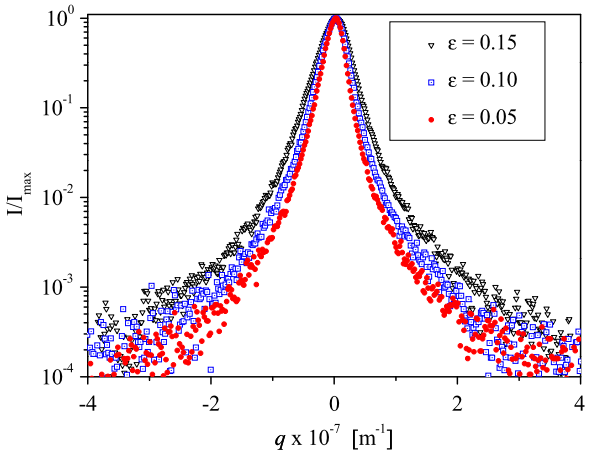

Fig. 4. 200 line profiles measured on Goss oriented, plane strain compressed Al–0.3%Mn single crystals.

Plane strain compression was carried out at a nominal strain rate of 10^{-3} s^{-1} to true (logarithmic) strains of 0.05, 0.10, and 0.15. Diffraction line profiles of the deformed single crystals have been measured using a PANalytical MRD diffractometer in high-resolution triple-axis mode. The incident beam of a sealed copper tube was monochromatized by a parabolic X-ray mirror coupled to a four-bounce Bartels monochromator preset for Cu-Kα_1 radiation. The diffracted beam was measured using a sealed proportional counter attached to an analyzer crystal with an angular acceptance of 12 arc seconds. This high resolution setup with negligible instrumental broadening is excellently suited for measurement of diffraction line profiles going to be analyzed according to the momentum method. Since plastic strain is small we expect in this case that grain subdivision is not severe and diffraction peak broadening will be mainly affected by dislocation induced strain broadening. The 200 peaks of the deformed samples are plotted in Fig. 4 as a function of reciprocal space variable q. The influence of plastic deformation is clearly visible, the higher is the plastic strain the broader are the peaks. The variance (Fig. 5(a)) and fourth order restricted moment (Fig. 5(b)) indicate additionally that the origin of this broadening should be related to the strain field of dislocations. The variance shows a clear linear behavior at large q (in a logarithmic q scale) with a slope (proportional to ρ) that is increasing with strain. The fourth order moments have a limit constant value (proportional to ρ), which also increases with applied strain. Evidently the coherent domain size is large, as the slope of the fitted line to the fourth order moment is nearly horizontal. It is worth emphasizing that the asymptotic behavior of the restricted moments differs from those obtained by Refs. [59–61] on uniaxially compressed [100]-oriented copper single crystals. In the present case the fourth order moment does not show any maximum at intermediate q values, a feature that has been related to a large dislocation density fluctuation in copper [59–61]. This indicates the existence of a more homogeneous dislocation structure in Al than in copper at room temperature.

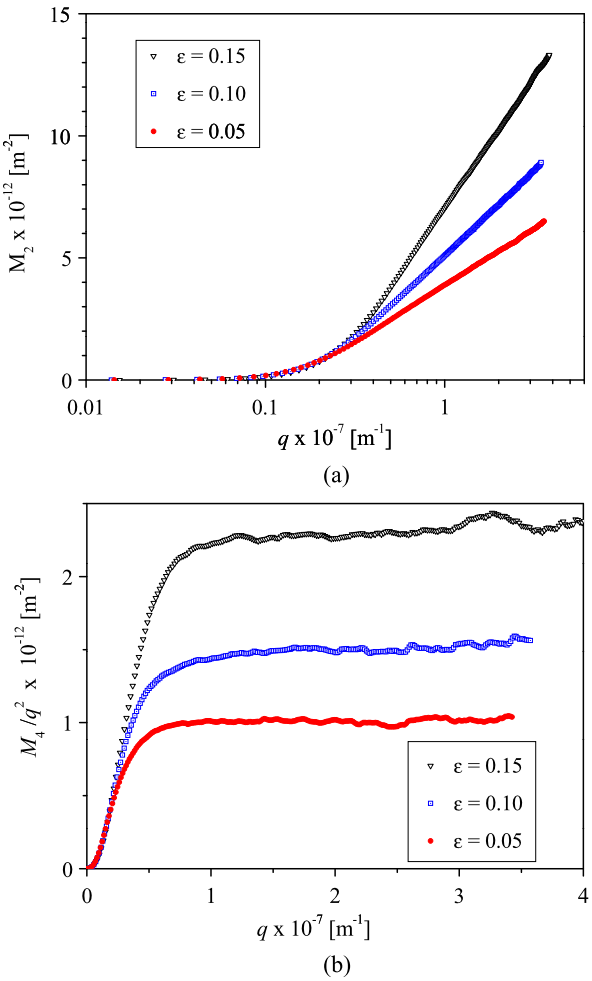

Fig. 5. Variance (a) and forth order moment (b) of the peaks shown in Fig. 4.

3.3. Single grain characterization in a polycrystal

The dislocation model of strain anisotropy proved to be a powerful method to obtain qualitative and quantitative data about the dislocation type, arrangement and density in single- and polycrystalline materials, especially when mainly one Burgers vector type is present in the crystal [73]. In hexagonal materials three Burgers vector types, $\langle a \rangle$, $\langle c \rangle$ and $\langle c + a \rangle$ and about 11 dislocation types are conceivable [74]. In a polycrystal the dislocation structure can vary from grain-to-grain depending on the orientation of the particular grain relative to the applied stress direction and on the stress state exerted by the neighborhood of the grain [75–78]. In the diffraction pattern of bulk polycrystalline materials the diffraction experiment carries out automatic averaging over a large ensemble of grains. This type of averaging obscures the detailed information about dislocation type, arrangement and density, and most probably provides only a messy mismatch about the prevailing dislocation structure in hexagonal materials. In recent experiments single grain diffraction was carried out on bulk polycrystalline specimens to obtain detailed microstructure data on the grain scale [35]. The method is the extension of the synchrotron experiment designed for structure and crystallographic orientation determination of bulk polycrystalline samples [79,80]. The thin rod-shape specimen is rotated at a slow rate in the monochromatic X-ray beam over a large ω range while the diffraction pattern is recorded a few hundred times by a fast detector. In the method described in [79,80] the sample to detector distance was about 200 mm which enabled to obtain the diffracted image in a wide reciprocal space range within a relatively short period of time. The specimen diameter and the beam cross-section are adjusted to acquire well separated diffraction spots at one time corresponding to individual grains in the specimen [80]. While the specimen is rotated over the ω axis the diffraction spots are coming-and-going. From the correlation between the ω settings of the specimen and the appearance of the diffraction spots these are correlated to specific grains and the grain orientations and positions in the specimen are determined [79,81]. The method was extended by placing the detector into additional positions far from the specimen in order to expand the angular resolution for the purpose of line profile analysis [35]. In the far position the detector was moved into several adjacent positions in order to cover a large enough reciprocal space

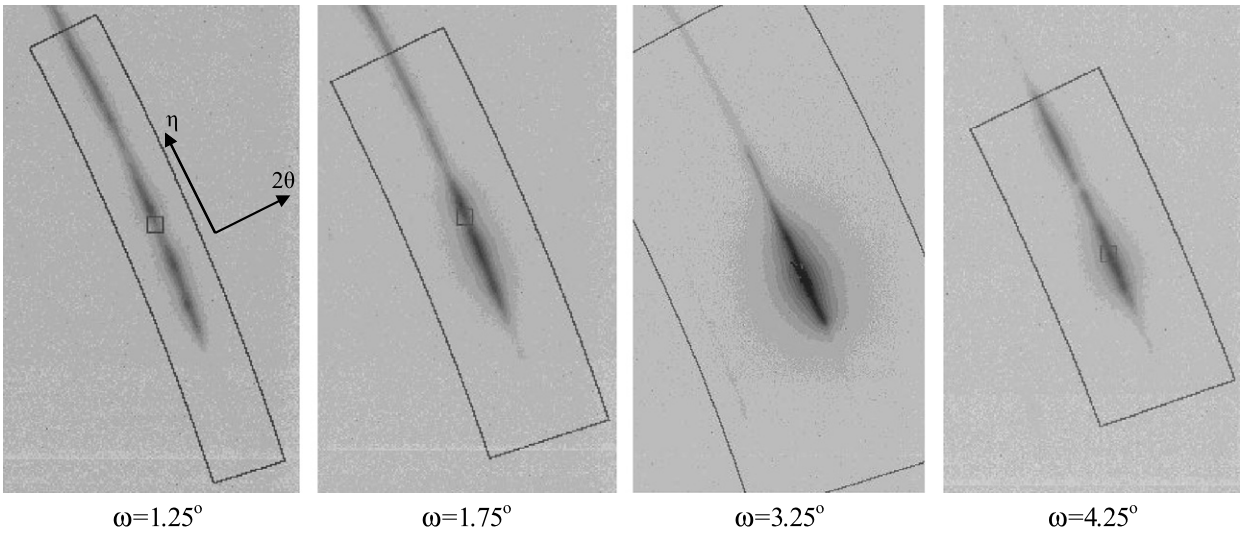

Fig. 6. Portions of four typical far-detector frames showing the integration procedure along the Debye–Scherrer arcs in the η direction. The large squares mark the highest intensity positions in the frames and the lines circumventing the diffraction spots are placed at distances of ±6-times and ±15-times the full-width-at-half-maximum (FWHM) of the peaks in the radial, i.e. 2θ, and in the η directions, respectively. Integration over the ω direction is done by summing up the frames over an ω range where the intensity falls off to 1% of the maximum intensity. For the peak shown here 12 subsequent ω frames have been summed up [35].

volume. The specimen rotation was repeated for the close and several far detector positions. The evaluation was carried out in several steps. In the first step the diffraction patterns at the close detector position were indexed and the grain orientations determined. In this procedure the ImageD11 [82] software was used.

The next step was the determination of the FWHM of the peaks in radial direction. The diffraction spots are 3-dimensional intensity distributions in reciprocal space: $I_{hk.l} = I(\eta, \omega, 2\theta)$, where η is the azimuth coordinate along the Debye–Scherrer arc, ω is the "rocking-curve" direction and 2θ is measured the "radial-direction" of the 2D detector. The microstrain, i.e. the mean square strain $\langle \varepsilon_L^2 \rangle$, produced by dislocations is provided by

$$I(2\theta) = \int I(\eta, \omega, 2\theta)\, \mathrm{d}\eta\, \mathrm{d}\omega \tag{7}$$

In the following we call $I(2\theta)$ the *line profile*. This is obtained by integrating the total intensity distribution corresponding to one diffraction spot over η and ω angles. Integration was carried out using an in-house developed image analysis software which is: (i) searching for the cohesive intensity maxima within the consecutive ω frames; and (ii) determines the η ranges for the same diffraction maxima in the same ω frames. Four typical ω frames selected from a cohesive series consisting of altogether 12 frames are shown in Fig. 6. The gray scale images show that the intensity is increasing and decreasing as the corresponding grain comes into and goes out of diffraction orientation. The integration over η is performed within the regions assigned by the black border lines and these results are summed up for each relevant ω frame. The qualitative feature of line broadening can be well seen in the Williamson-Hall (WH) plot of the FWHM values of line profiles. A typical WH plot for one of the grains is shown in Fig. 7(a). The data show that the breadths are different for different orientations even for the same $|\boldsymbol{g}|$ value. The diffraction profiles were evaluated by the eCMWP method for obtaining the *measured* individual dislocation contrast factors $C_{individ}^{meas}$, for each reflection [35].

The last step was to find the dislocation type and Burgers vectors existing in the investigated individual grains. This was carried out by finding the best match between the measured and theoretically calculated and possible, $C_{individ}^{meas}$ and C_{theor} contrast factors. The theoretical contrast factors were determined by using the ANIZC [68] software. The best correlation between the measured and theoretical contrast factors for the grain shown here was found for the $\langle c + a \rangle$ type screw dislocations with the Burgers vector type: $\langle 2113 \rangle$ [35]. The qualitative cross-check of the dislocation type determined by this procedure is provided by the *modified* WH plot [83] in which the breadth values are plotted versus $KC^{1/2}$ instead of K, as shown in Fig. 7(b). Here the contrast factors, C are those corresponding to the dislocations providing the best match. The rearrangement of the FWHM values along a straight or smooth curve indicates that the selection of the dislocations is with great certainty the correct one.

3.4. Characterization of texture components in plastically deformed Al–0.5%Mg polycrystals

The above presented single grain method can be extended to an ensemble of grains that belong to a given texture component. These grains have very similar crystallographic orientations. The proposed approximation will be valid as the proportion of "randomly" oriented grains is much smaller than that of different texture components, a condition better

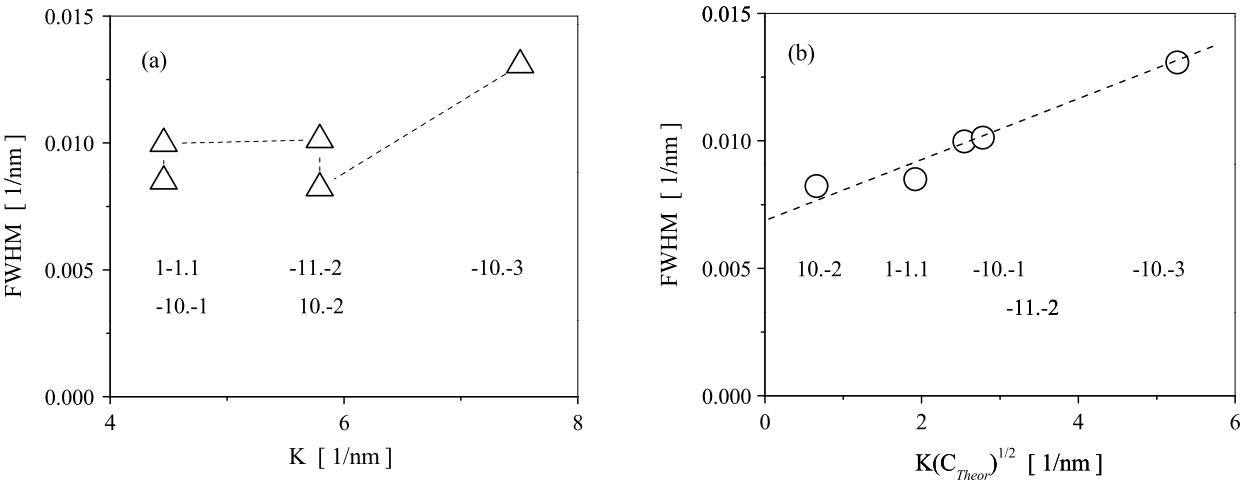

Fig. 7. Typical Williamson-Hall (a) and *modified* Williamson-Hall (b) plots for one grain. The data show that the breadths are different for different orientations even for the same $|\boldsymbol{g}|$ values. In the *modified* Williamson-Hall plot the theoretical dislocation contrast factors correspond to $\langle c+a\rangle$ type screw dislocations. (By courtesy of [35].)

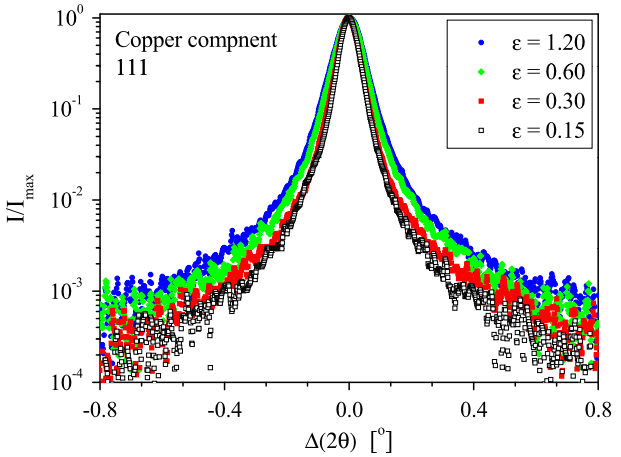

Fig. 8. Line profiles measured on the grains of the copper texture component in plane strain compressed Al–0.5%Mg polycrystals.

fulfilled by highly deformed structures. For investigations small polycrystalline blocks of $10 \times 10 \times 7$ mm^3 in size were machined by spark erosion from a recrystallized Al–0.5%Mg alloy and deformed in channel die compression at room temperature until logarithmic strains of 0.15, 0.30, 0.60 and 1.20. It is known that plane strain compression leads to the formation at high strains of the following five texture components: Cube (001)[100], Goss (110)[001], Brass (110)[-112], Copper (112)[11-1] and S (123)[41-2], which have been investigated by X-ray line profile analysis. High-resolution diffraction peaks were measured using a double-crystal diffractometer equipped with a Ge-440 monochromator tuned for the Co-$K\alpha_1$ line. To access the grains corresponding to the different texture components the samples have been cut parallel to the reflecting *hkl* planes and oriented in the goniometer in symmetrical diffraction geometry (see, for example, Fig. 1 in [84]). Each texture component has been characterized by two diffraction vectors, carefully selected in order to avoid overlapping with diffraction vectors of the same *hkl* order, but which could belong to other texture components.

High-resolution 11-1 peaks (Fig. 8) measured on grains of the Copper texture component indicate a gradual increase of peak broadening with applied strain. The effect is visible as well on peaks corresponding to other components, too (not shown here). To highlight the differences in dislocation structure between deformed single and polycrystals we apply again the momentum method (Eqs. (4) and (5)). Figs. 9(a) and 9(b) show the variance and the fourth order moment, respectively, for the Copper peak corresponding to the sample with 0.15 strain. Their visual checking clearly indicates that the asymptotic behavior of both moments is linear with q. In other words, additionally to dislocation strain, peak broadening is also affected by a small domain size. Since size broadening is the dominant contribution, the third and higher order contributions (like the term containing the taper parameter T in Eq. (4) or the third and forth terms in Eq. (5)) cannot be satisfactorily determined and should be set equal to zero for the fit. The q interval used during the evaluation of the variance and fourth order moment is indicated by the two arrows (Figs. 9(a) and 9(b)). It is remarkable that the sum of the linear and

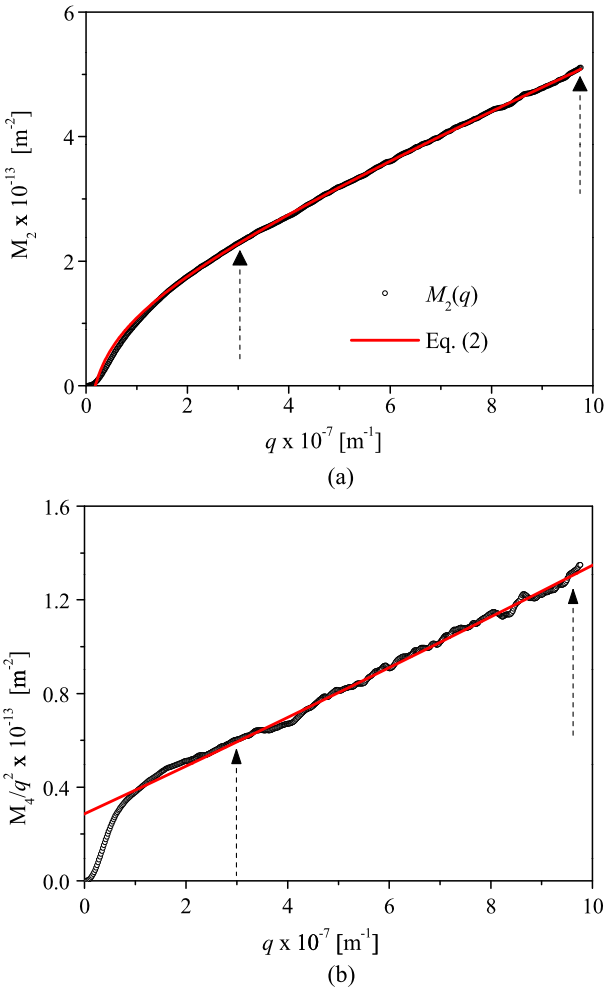

Fig. 9. Variance (a) and forth order moment (b) of the copper peak at a strain of 0.15.

logarithmic function (Eq. (4)) describes the variance in almost the entire q range (red curve). It is important to mention that since the fitting function contains only three parameters (the formal dislocation density ($\rho^* = \Lambda\langle\rho\rangle$), the coherent domain size (ε_F) and q_0) and the number of data points exceeds 100 the results of the fit have a small statistical error. The situation is even better for the parameters determined from the fourth order moment containing just ρ^* and ε_F. Since both moments contain the same parameters a cross check of the results becomes possible. In practice the background is slowly varied until nearly identical values of ρ^* and ε_F are obtained from the two moments [20,67].

Evaluation of the true dislocation density should consider the value of the dislocation contrast factor "C", which can be numerically calculated for given dislocation types (edge, screw or mixed) and dislocation configurations using ANIZC [68]. Since dislocation contrast is related to the elastic strain field of dislocations, which are linear crystal defects, the contrast depends on the relative orientation between the diffraction vector and the displacement field vector of the dislocation as well as on the elastic anisotropy of the crystal [14,17]. In case when several slip systems are activated the average C factor of a given *hkl* diffraction vector will not deviate much from the contrast factor corresponding to a powder specimen (when an additional averaging over similar *hkl* vectors is performed). As the elastic anisotropy factor of Al is small (~ 1.2) the above statement is true for the present case of the present Al alloy and in a first order approximation we can calculate the true dislocation densities using the average contrast factors of a powder specimen. It is important to note that averaging over all *hkl* vectors of the same order is equivalent to averaging over all slip systems for one given *hkl*. We show that the suggested approximation does not change the general conclusion of present subsection related to the heterogeneity of plastic slip in different texture components. Evidently, better approximations for average C calculation, based on crystal plasticity simulations or complementary TEM studies also exist [84–86].

Fig. 10(a) shows the variation of the dislocation density and coherent domain size in grains of the brass texture component as a function of strain. The results are average values obtained from the 1-11 and 002 diffraction peaks. Compared to the single crystal case (Figs. 5(a) and 5(b)), when the coherent domain size at 0.15 strain is still very large, deformation of polycrystal grains leads to a more structured dislocation arrangement, characterized by a smaller coherent domain size.

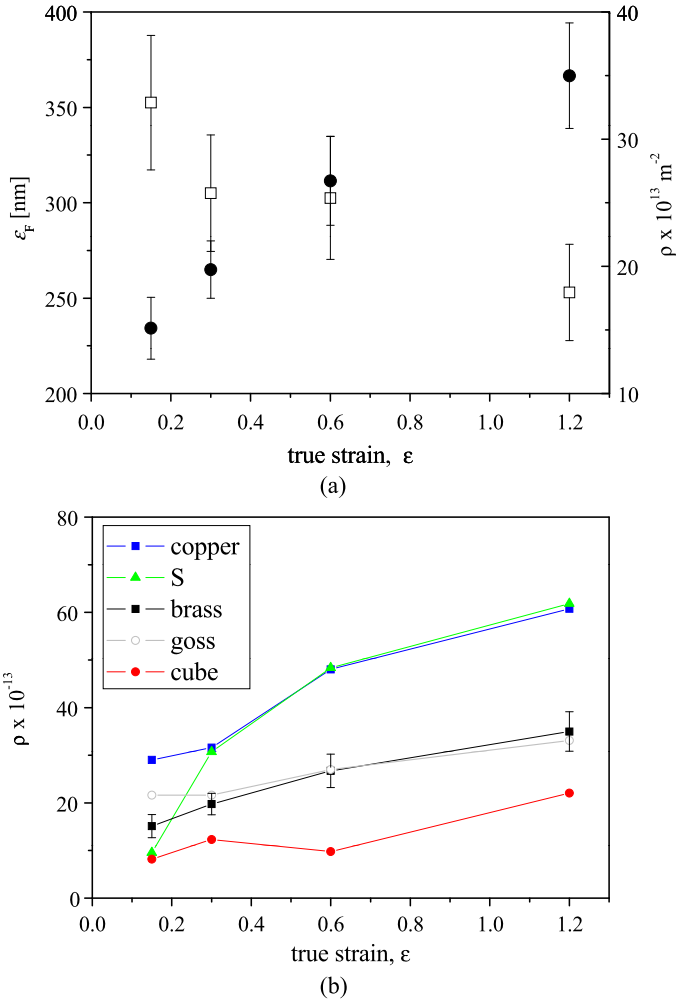

Fig. 10. Variation of dislocation density and coherent domain size in the brass texture component as a function of strain (a), and variation of dislocation density in five texture components of the Al–0.5Mg alloy (b).

Fig. 10(b) summarizes the dislocation density data for the five texture components investigated. According to it the highest dislocation density develops in the *S* and Copper, it is intermediate in the Brass and Goss and is the smallest in the Cube component. This ranking is different from the one observed during hot-rolling at 400 °C of an Al–2.5Mg alloy [85,86]. In hot-rolling the *S* component showed the highest dislocation density, while all other four had nearly identical values [86].

4. Conclusions

The theoretical basis and application of line profile analysis to crystals with volumetric, planar and linear lattice defects has been presented. Two bottom-up evaluation methods have been introduced and exemplified on differently broadened line profiles. The momentum method gives highly accurate values for the coherent domain size and dislocation density. The fluctuation of the dislocation density can be evaluated if the coherent domain size is infinite, practically larger than 1 μm. The momentum method, however, cannot be applied to diffraction patterns with overlapping peaks. The eCMWP procedure due to the convolutional approach allows a more general evaluation is terms of many possible defects and can handle overlapping peaks, too.

The two methods have been exemplified on plastically deformed single and polycrystals. It has been shown that at intermediate strains (0.15) the dislocation structure formed in polycrystalline Al–0.5Mg alloy is more heterogeneous than the structure in the single crystal of Al–0.3Mn. Applying the modified Williamson-Hall analysis of peak widths recorded in transmission geometry at synchrotron source has allowed determining the active slip systems in single grains well embedded in the bulk of a polycrystalline sample. Evidently, the high energy synchrotron radiation has several advantages, which seem to determine forthcoming developments in line profile analysis. It is expected that in situ tests on deeply embedded grains in the polycrystal will reveal new aspects of polycrystal plasticity.

References

[1] H.M. Rietveld, Acta Cryst. 22 (1967) 151–152.
[2] J.I. Langford, in: S. Block, C.R. Hubbard (Eds.), Accuracy in Powder Diffraction, in: NBS Special Publication, vol. 567, National Bureau of Standards, Washington DC, 1980, p. 255.
[3] R.A. Young, D.B. Wiles, J. Appl. Cryst. 15 (1982) 430–438.
[4] M. Ahtee, L. Unonius, M. Nurmela, P. Suortti, J. Appl. Cryst. 17 (1984) 352–357.
[5] H. Toraya, J. Appl. Cryst. 19 (1986) 440–447.
[6] J.I. Langford, R. Delhez, Th.H. de Keijser, E.J. Mittemeijer, Aust. J. Phys. 41 (1988) 173–187.
[7] D. Balzar, J. Appl. Cryst. 28 (1995) 244–245.
[8] D. Balzar, in: R.L. Snyder, H.J. Bunge, J. Fiala (Eds.), Defect and Microstructure Analysis from Diffraction, in: IUCr Monographs on Crystallography, vol. 10, Oxford University Press, New York, 1999, p. 94.
[9] A.R. Stokes, A.J.C. Wilson, Proc. Cambridge Philos. Soc. 38 (1942) 313–322.
[10] B.E. Warren, B.L. Averbach, J. Appl. Phys. 21 (1950) 595–597.
[11] E.F. Bertaut, Acta Cryst. 3 (1950) 14–18.
[12] M.A. Krivoglaz, K.P. Rjaboshapka, Fiz. Metallov Metalloved. 15 (1963) 18–31.
[13] M.A. Krivoglaz, Theory of X-ray and Thermal Neutron Scattering by Real Crystals, Springer-Verlag, Berlin, 1996.
[14] M. Wilkens, Phys. Stat. Sol. (a) 2 (1970) 359–370.
[15] M. Wilkens, in: J.A. Simmons, R. de Wit, R. Bullough (Eds.), Fundamental Aspects of Dislocation Theory, vol. II, Spec. Publ. No. 317, Nat. Bur. Stand. (US), Washington, DC, USA, 1970, p. 1195.
[16] I. Gaál, in: N.H. Andersen, et al. (Eds.), Proc. 5th Riso Int. Symp. Met. Mat. Sci., Risø Nat. Lab., Roskilde, Denmark, 1984, pp. 245–254.
[17] I. Groma, T. Ungár, M. Wilkens, J. Appl. Cryst. 21 (1989) 47–53.
[18] T. Ungár, I. Groma, M. Wilkens, J. Appl. Cryst. 22 (1989) 26–34.
[19] I. Groma, Phys. Rev. B 57 (1998) 7535–7542.
[20] A. Borbély, I. Groma, Appl. Phys. Lett. 79 (2001) 1772–1774.
[21] L. Velterop, R. Delhez, Th.H. de Keijser, E.J. Mittemeijera, D. Reefman, J. Appl. Cryst. 33 (2000) 296–306.
[22] E. Estevez-Rams, A. Penton-Madrigal, R. Lora-Serrano, J. Martinez-Garcia, J. Appl. Cryst. 34 (2001) 730–736.
[23] P. Scardi, M. Leoni, Acta Cryst. A 58 (2002) 190–200.
[24] E. Estevez-Rams, M. Leoni, P. Scardi, B. Aragon-Fernandez, H. Fuess, Phil. Mag. A 83 (2003) 4045–4057.
[25] M.M.J. Treacy, J.M. Newsam, M.W. Deem, Proc. Roy. Soc. London A 433 (1991) 499–520.
[26] T. Ungár, I. Dragomir, Á. Révész, A. Borbély, J. Appl. Cryst. 32 (1999) 992–1002.
[27] T. Ungár, J. Gubicza, G. Ribárik, A. Borbély, J. Appl. Cryst. 34 (2001) 298–310.
[28] L. Balogh, G. Ribárik, T. Ungár, J. Appl. Phys. 100 (2006) 023512.
[29] L. Balogh, G. Tichy, T. Ungár, J. Appl. Cryst. 42 (2009) 580–591.
[30] G. Ribárik, T. Ungár, J. Gubicza, J. Appl. Cryst. 34 (2001) 669–676.
[31] T. Ungár, H. Mughrabi, M. Wilkens, Acta Metall. 30 (1982) 1861–1867.
[32] T. Ungár, H. Mughrabi, D. Rönnpagel, M. Wilkens, Acta Metall. 32 (1984) 333–342.
[33] E. Schafler, K. Simon, S. Bernstorff, P. Hanák, G. Tichy, T. Ungár, M.J. Zehetbauer, Acta Mater. 53 (2005) 315–322.
[34] P. Cordier, T. Ungár, L. Zsoldos, G. Tichy, Nature 428 (2004) 837–840.
[35] T. Ungár, G. Ribárik, L. Balogh, A.A. Salem, S.L. Semiatin, G. Vaughan, Scripta Mater. 63 (2010) 69–72.
[36] P. Scardi, M. Leoni, in: E.J. Mittemeijer, P. Scardi (Eds.), Diffraction Analysis of the Microstructure of Materials, in: Springer Ser. Mater. Sci, vol. 68, Springer-Verlag, Berlin, 2004, p. 51.
[37] G. Ribárik, J. Gubicza, T. Ungár, Mater. Sci. Eng. A 387–389 (2004) 343–347, a free software can be found at the homepage: http://www.renyi.hu/cmwp.
[38] P. Scardi, M. Leoni, Acta Mater. 53 (2005) 5229–5239.
[39] R.W. James, The Optical Principles of the Diffraction of X-Rays, G. Bell and Sons, Ltd., London, 1965.
[40] P. Scardi, M. Leoni, R.J. Delhez, J. Appl. Cryst. 37 (2004) 381–390.
[41] J.I. Langford, D. Louër, Rep. Progr. Phys. 59 (1996) 131–234.
[42] Ch.D. Terwilliger, Y.M. Chiang, Acta Metall. Mater. 43 (1995) 319–328.
[43] C.E. Krill, R. Birringer, Phil. Mag. A 77 (1998) 621–640.
[44] M. Leoni, P. Scardi, J. Appl. Cryst. 37 (2004) 629–634.
[45] A.J.C. Wilson, X-ray Optics, 2nd ed., Methuen, London, 1962.
[46] A.J.C. Wilson, Proc. Phys. Soc. 80 (1962) 286.
[47] A.J.C. Wilson, Proc. Phys. Soc. 81 (1963) 41.
[48] J.I. Langford, A.J.C. Wilson, J. Appl. Cryst. 11 (1978) 102–113.
[49] J.I. Langford, D. Louër, P. Scardi, J. Appl. Cryst. 33 (2000) 964–974.
[50] N.C. Popa, D. Balzar, J. Appl. Cryst. 35 (2002) 338–346.
[51] B. Clausen, C.N. Tome, D.W. Brown, S.R. Agnew, Acta Mater. 56 (2008) 2456–2468.
[52] L. Wu, S.R. Agnew, D.W. Brown, G.M. Stoica, B. Clausen, A. Jain, D.E. Fielden, P.K. Liaw, Acta Mater. 56 (2008) 3699–3707.
[53] W. Massa, S. Wocadlo, S. Lotz, K.Z. Dehnicke, Anorg. Allg. Chem. 589 (1990) 79–88.
[54] http://metal.elte.hu/~evente/stacking.
[55] B.E. Warren, X-Ray Diffraction, Dover Publications, New York, 1990.
[56] B.E. Warren, B.L. Averbach, J. Appl. Phys. 23 (1952) 497–498.
[57] V.M. Kaganer, R. Köhler, M. Schmidbauer, R. Opitz, B. Jenichen, Phys. Rev. B 55 (1997) 1793–1810.
[58] M. Wilkens, K. Hertz, H. Mughrabi, Z. Metallk. 71 (1980) 376.
[59] F. Székely, I. Groma, J. Lendvai, Phys. Rev. B 62 (2000) 3093–3098.
[60] F. Székely, I. Groma, J. Lendvai, Mat. Sci. Eng. A 309 (2001) 352–355.
[61] F. Székely, I. Groma, J. Lendvai, Scripta Mater. 45 (2001) 55–60.
[62] I. Groma, G. Monnet, J. Appl. Cryst. 35 (2002) 589–593.
[63] H. Mughrabi, T. Ungár, W. Kienle, M. Wilkens, Phil. Mag. A 53 (1986) 793–813.
[64] B. Jakobsen, H.F. Poulsen, U. Lienert, W. Pantleon, Acta Mater. 55 (2007) 3421–3430.
[65] R. Barabash, Mat. Sci. Eng. A 309–310 (2001) 49–54.
[66] A. Borbély, C. Maurice, J.H. Driver, J. Appl. Cryst. 41 (2008) 747–753.
[67] A. Borbély, A. Révész, I. Groma, Z. Kristallogr. Suppl. 23 (2006) 87–92.
[68] A. Borbély, J. Dragomir, G. Ribarik, T. Ungár, J. Appl. Cryst. 36 (2003) 160–162, a free computer program is available at: http://metal.elte.hu/anizc.

[69] N.C. Popa, J. Appl. Cryst. 31 (1998) 176–180.
[70] T. Ungár, G. Tichy, Phys. Stat. Sol. A 147 (1999) 425–434.
[71] K. Máthis, K. Nyilas, A. Axt, I.D. Cernatescu, T. Ungár, P. Lukáč, Acta Mater. 52 (2004) 2889–2894.
[72] K. Máthis, F. Chmelík, Z. Trojanová, P. Lukáč, J. Lendvai, Mat. Sci. Eng. A 387–389 (2004) 331–335.
[73] T. Ungár, J. Powder Diffr. 23 (2008) 125–132.
[74] I.P. Jones, W.B. Hutchinson, Acta Metall. 29 (1981) 951–968.
[75] P.G. Partridge, Metallurg. Rev. 118 (1968) 169–193.
[76] M.P. Miller, J.S. Park, P.R. Dawson, T.S. Han, Acta Mater. 56 (2008) 3927–3939.
[77] S. Merkel, C.N. Tomé, H.R. Wenk, Phys. Rev. B 79 (2009) 064110.
[78] R.A. Lebensohn, C.N. Tome, P. Castaneda, Proc. Phil. Mag. 87 (2007) 4287–4322.
[79] E.M. Lauridsen, S. Schmidt, R.M. Suter, H.F. Poulsen, J. Appl. Cryst. 34 (2001) 744–750.
[80] D. Juul Jensen, E.M. Lauridsen, L. Margulies, H.F. Poulsen, S. Schmidt, H.O. Sørensen, G.B.M. Vaughan, Mater. Today 9 (2006) 18–25.
[81] X. Fu, H.F. Poulsen, S. Schmidt, S.F. Nielsen, E.M. Lauridsen, D. Juul Jensen, Scripta Mater. 49 (2003) 1093–1096.
[82] J. Wright, ImageD11, http://sourceforge.net/projects/fable/files/ImageD11/.
[83] T. Ungár, A. Borbély, Appl. Phys. Lett. 69 (1996) 3173–3175.
[84] A. Borbély, J.H. Driver, T. Ungár, Acta Mater. 48 (2000) 2005–2016.
[85] A. Borbély, G. Guiglionda, J.H. Driver, Z. Metallk. 93 (2002) 689–693.
[86] G. Guiglionda, A. Borbély, J.H. Driver, Acta Mater. 52 (2004) 3413–3423.